

Exchange-Induced Upconversion in $\text{Rb}_2\text{MnCl}_4\text{:Yb}^{3+}$

Christine Reinhard, Rafael Valiente, and Hans U. Güdel*

Departement für Chemie und Biochemie, Universität Bern, Freiestrasse 3, CH-3000 Bern 9, Switzerland

Received: February 7, 2002; In Final Form: May 3, 2002

Crystals of Yb^{3+} doped Rb_2MnCl_4 exhibit very intense yellow-orange $\text{Mn}^{2+} {}^4\text{T}_{1g} \rightarrow {}^6\text{A}_{1g}$ upconversion luminescence under near-infrared ${}^2\text{F}_{7/2} \rightarrow {}^2\text{F}_{5/2}$ Yb^{3+} excitation around $1\ \mu\text{m}$ at 15 K. Excitation with 10 ns pulses indicates that the upconversion process consists of a sequence of ground-state and excited-state absorption steps. The upconversion mechanism is cooperative, involving both Yb^{3+} and Mn^{2+} ions in the crystal, and we postulate an exchange mechanism between adjacent Yb^{3+} and Mn^{2+} ions to account for the unusually high efficiency of the process. The efficiency of the upconversion process is dependent on the nature of the $\text{Yb}^{3+}\text{--Mn}^{2+}$ connectivity. The upconversion in $\text{Rb}_2\text{MnCl}_4\text{:Yb}^{3+}$, with a linear $\text{Yb}^{3+}\text{--Cl}^-\text{--Mn}^{2+}$ arrangement, is 3 orders of magnitude more efficient than in the $\text{Yb}^{3+}\text{--}(\text{Br}^-)_3\text{--Mn}^{2+}$ arrangement of face-sharing octahedra in $\text{CsMnBr}_3\text{:Yb}^{3+}$.

1. Introduction

Photon upconversion from the near-IR (NIR) to the visible (VIS) is potentially interesting for many applications. The well-known process of second-harmonic generation in nonlinear optical materials is widely used for the conversion of NIR laser radiation into VIS or UV radiation. It requires coherent radiation. In this paper we are talking about a different nonlinear upconversion (UC) process, which does not require coherent radiation. Instead, it requires the existence of a metastable intermediate state in the NIR, which is reached with the first photon. The second photon then promotes the system to a higher excited state, followed by emission from a second metastable state in the VIS. The first UC step can be followed by a second and third UC step, if there exist metastable states at higher energies.

Since the early reviews by Auzel¹ and Wright² about UC processes, there has been a lot of work on UC processes and UC materials. Both fundamental studies of new materials and the mechanisms of upconversion and investigations of the application potential of the UC process have been reported. These potential applications are in the areas of lighting, lasers, displays, and imaging systems as well as NIR photon counters.^{3–5} Most of this work is based on lanthanide-doped crystals and glasses. f–f excited states of lanthanides are often metastable because of the shielding of the f-electrons and the resulting small electron–phonon coupling. Er^{3+} , Tm^{3+} , Nd^{3+} , and Ho^{3+} are the most frequently used activator ions for upconversion processes.^{6–9} Very often, Yb^{3+} is used as a sensitizer. This ion plays a very special part among the lanthanides because of its $(4f)^{13}$ electron configuration. Besides the ${}^2\text{F}_{7/2}$ ground multiplet, there is only one excited f–f multiplet ${}^2\text{F}_{5/2}$ around $1\ \mu\text{m}$. In the rest of the NIR and the full VIS part of the spectrum, Yb^{3+} oxide and halide compounds are transparent. Yb^{3+} is thus an ideal sensitizer because it does not interfere with the UC processes of the activator. VIS lasers and phosphors based on $\text{Yb}^{3+}/\text{Er}^{3+}$ and $\text{Yb}^{3+}/\text{Tm}^{3+}$ codoped materials excited by UC into ${}^2\text{F}_{5/2}$ of Yb^{3+} have been reported.^{10,11}

In our research on new upconversion processes and materials, we use a chemical approach. By varying the chemical composition and structure of the compounds, we vary and tune the UC light emission properties. Using heavy halides such as chlorides and bromides instead of the commonly used oxides and fluorides, we reduce the phonon energies and thus reduce the efficiency of multiphonon relaxation processes. In lanthanide-doped materials, this leads to new UC luminescences.^{12–15} We are also exploring UC processes in transition-metal (TM) doped crystals. As a result of the stronger electron–phonon coupling than in lanthanide compounds, multiple metastable excited states are rare in TM doped crystals. We have observed UC phenomena in Ti^{2+} ($3d^2$), Ni^{2+} ($3d^8$), Mo^{3+} ($4d^3$), Re^{4+} ($5d^3$), and Os^{4+} ($5d^4$) doped halides.^{16–20} Very recently, we have started to combine TM and lanthanide ions in the same crystal, with very new and surprising results. Yb^{3+} doped RbMnCl_3 , CsMnCl_3 , and CsMnBr_3 crystals emitted visible light upon NIR excitation of Yb^{3+} around $1\ \mu\text{m}$ at cryogenic temperatures.^{21–24} Similarly, in Cr^{3+} and Yb^{3+} codoped garnets ${}^2\text{E}$ emission of Cr^{3+} in the red could be induced by $1\ \mu\text{m}$ Yb^{3+} excitation at low temperatures.²⁵

The present study falls into the category of Yb^{3+} doped Mn^{2+} halide compounds. In references 21 and 22 it was found that at least two different mechanisms are at work in this new type of upconversion process. It was also found that the efficiency of the process varied by 3 orders of magnitude in the various compounds for comparable experimental conditions. The reason for this variation is not understood. The main objective of the present study is to shed more light on this important question of how the UC efficiency relates to the chemical composition and the structure of the compounds. In CsMnBr_3 , the Yb^{3+} ions replace octahedrally coordinated Mn^{2+} ions, and they share an octahedral face with neighboring Mn^{2+} ions. In RbMnCl_3 and CsMnCl_3 , the situation is less clear because there are both face-sharing and corner-sharing $\text{Mn}^{2+}\text{--Mn}^{2+}$ connections in the lattice. In Rb_2MnCl_4 , the situation is clear again. It crystallizes in the tetragonal K_2NiF_4 layer perovskite structure with space group $I4/mmm$,²⁶ and all the $\text{Mn}^{2+}\text{--Mn}^{2+}$ connections are corner-sharing. The connections of the incorporated Yb^{3+} ion with the lattice are thus linear $\text{Yb}^{3+}\text{--Cl}^-\text{--Mn}^{2+}$ units. From a

* To whom correspondence should be addressed. E-mail: hans-ulrich.guedel@iac.unibe.ch. Fax: +41 31 631 43 99.

comparison of the UC behavior in the title compound with the other lattices, we expect to establish an empirical correlation between the UC behavior and the bridging geometry.

2. Experimental Section

2.1 Crystal Growth. Single crystals of Yb^{3+} doped Rb_2MnCl_4 were grown from the melt by the Bridgman technique using stoichiometric amounts of RbCl and MnCl_2 with a nominal doping concentration of 1 mol % YbCl_3 , as described elsewhere.²⁷ Following this procedure, single crystals of centimeter size and high optical quality were obtained. The actual Yb^{3+} concentration in Rb_2MnCl_4 crystals is less than 0.1%. This follows from our inability to measure any $^2\text{F}_{7/2} \rightarrow ^2\text{F}_{5/2}$ absorption lines at 12 K, even in a crystal of 8-mm thickness. The crystals are air sensitive and must be handled and stored in inert atmosphere or in paraffin oil. They cleave easily perpendicular to the tetragonal *c* axis. Crystals were oriented under the polarizing microscope.

2.2 Spectroscopy. Absorption spectra were measured on a Cary 5e (Varian) spectrometer with *E*/*c* (π), and axial (α), that is, unpolarized with the beam along the *c* axis perpendicular to the well-developed faces. For the π spectrum, a crystal was imbedded in polymerizable resin and then cut and polished parallel to the *c* axis. The samples were mounted in a closed copper cell and cooled with a closed cycle cryostat (Air Products Displex).

Continuous-wave Yb^{3+} luminescence spectra, Mn^{2+} upconversion, and excitation measurements were performed using a tunable Ti:sapphire laser (Spectra Physics 3900S), pumped by an argon-ion laser (Spectra Physics 2060-10SA) as an excitation source. Wavelength control was achieved by an inchworm driven (Burleigh PZ-501) birefringent filter, and the wavelength was monitored with a wavemeter (Burleigh WA2100). The sample luminescence was dispersed by a 0.85 m double monochromator (Spex 1402) with 500 nm blazed 1200 grooves/mm gratings. The luminescence was detected by a cooled photomultiplier tube (RCA C31034 or Hamamatsu 3310-01) using a photon-counting system (Stanford Research SR400). The laser beam (diameter: 1 mm) was focused on the sample with an *f* = 53-mm focal lens. Mn^{2+} luminescence was directly excited using the 514.5 nm line of an Ar^+ laser. The sample luminescence was dispersed by a 0.75 m single monochromator (Spex 1702) equipped with a 750 nm blazed 600 grooves/mm grating.

All the luminescence spectra were corrected for the wavelength-dependent response of the monochromator and detection system and for the refractive index of air (vacuum correction). The upconversion excitation spectrum was corrected for the square of the wavelength-dependent output power of the Ti:sapphire laser. The VIS and NIR luminescence spectra excited in the NIR are scaled to an excitation power of 191 mW. The upconversion VIS luminescence is scaled as the square, and the downconversion NIR luminescence is scaled linearly as a function of the excitation power of the laser. The luminescence intensities are not corrected for the temperature-dependent absorption cross sections at the excitation energies.

For Yb^{3+} luminescence lifetime measurements in the NIR, rectangular pulses of the Ti:sapphire were generated by using an acousto-optic modulator (Coherent 305) connected to a function generator (Stanford Research DS 345). The temporal behavior of the luminescence intensity was detected using a multichannel scaler (Stanford Research SR430) for decay curves. For the upconversion luminescence transient measurement, 10 ns pulses of a dye laser (Lambda Physik FL3002; Pyridine 1 in methanol) pumped by the second harmonic of a Nd: YAG

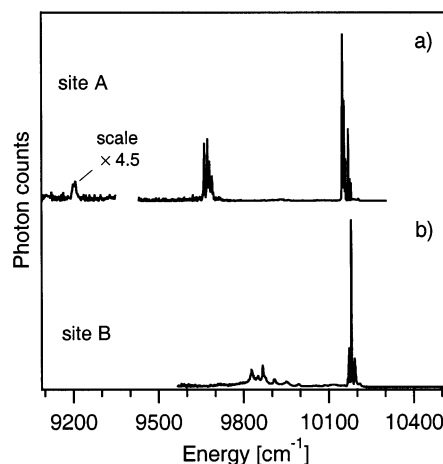


Figure 1. 15 K $^2\text{F}_{5/2} \rightarrow ^2\text{F}_{7/2}$ luminescence spectra of $\text{Rb}_2\text{MnCl}_4:\text{Yb}^{3+}$ excited site selectively at (a) 10910 cm^{-1} (site A) and (b) 10777 cm^{-1} (site B).

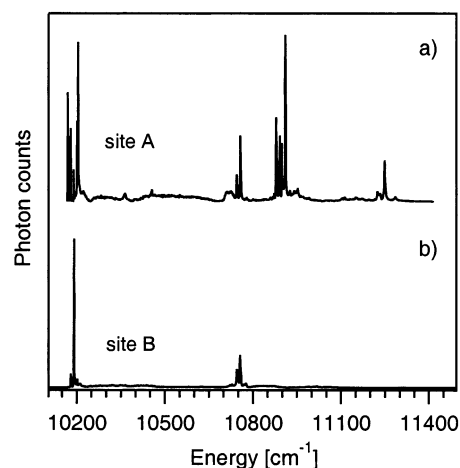


Figure 2. 15 K excitation spectra (corrected for the wavelength-dependent output power of the Ti:sapphire laser) monitoring the $^2\text{F}_{5/2} \rightarrow ^2\text{F}_{7/2}$ luminescence at (a) 10152 cm^{-1} and (b) 9870 cm^{-1} .

(Quanta Ray DCR 3) were Raman shifted (Quanta Ray, RS-1, H_2 , 340 psi, operative range 935–1025 nm). For Mn^{2+} luminescence lifetime measurements, the 532 nm second harmonic of the Nd:YAG was used. For all the luminescence measurements, cooling of the crystals was achieved using the helium-gas flow technique.

3. Results

Figure 1 shows NIR luminescence spectra in the 1 μm region at 15 K of $\text{Rb}_2\text{MnCl}_4:\text{Yb}^{3+}$. Two different luminescence spectra were obtained depending on the excitation energy. The spectra in Figure 1a and 1b were excited at 10910 and 10777 cm^{-1} , respectively. The corresponding excitation spectra are shown in Figure 2a and 2b, respectively. All the spectra consist of sharp lines and correspond to *f*–*f* transitions of Yb^{3+} . It will be shown in section 4.1 that the spectra in Figures 1a/2a and 1b/2b correspond to two Yb^{3+} sites designated A and B, respectively.

Figure 3 shows 15 K luminescence spectra of $\text{Rb}_2\text{MnCl}_4:\text{Yb}^{3+}$ excited at 19455 cm^{-1} (3a), 10910 cm^{-1} (3b), and 10777 cm^{-1} (3c). They all exhibit a broad luminescence band in the orange part of the spectrum which is readily assigned to $^4\text{T}_{1g} \rightarrow ^6\text{A}_{1g}$ of Mn^{2+} . Its position slightly depends on the excitation: In Figure 3a and 3b it is essentially the same, peaking at about 16200 cm^{-1} , whereas in 3c it is red-shifted by about 340

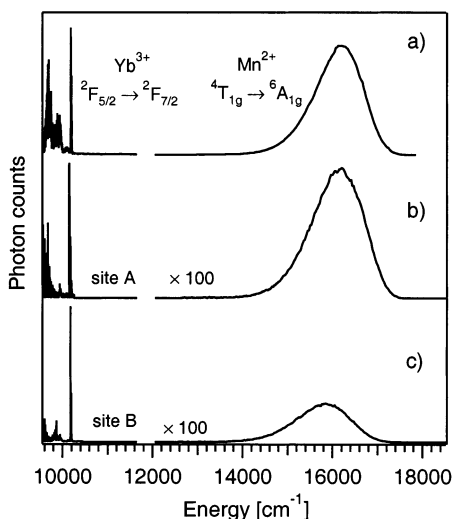


Figure 3. Survey luminescence and upconversion luminescence spectra at 15 K of $\text{Rb}_2\text{MnCl}_4:\text{Yb}^{3+}$ excited at (a) 19455 cm^{-1} (b) 10910 cm^{-1} (site A) (c) 10777 cm^{-1} (site B) for an excitation power of 191 mW. Note magnification of the upconverted $\text{Mn}^{2+} {}^4\text{T}_{1g} \rightarrow {}^6\text{A}_{1g}$ luminescence by a factor of 100.

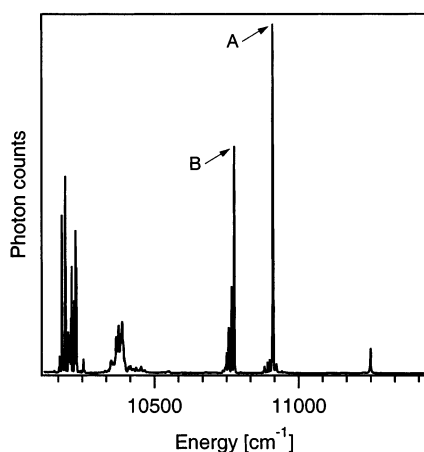


Figure 4. 15 K excitation spectrum monitoring the yellow-orange $\text{Mn}^{2+} {}^4\text{T}_{1g} \rightarrow {}^6\text{A}_{1g}$ upconversion luminescence at 16000 cm^{-1} . The spectrum is corrected for the square of the wavelength-dependent excitation power of the Ti:sapphire laser. The arrows A and B denote the excitation energy used in the upconversion experiments.

cm^{-1} . The three spectra of 3a, 3b, and 3c excited in the NIR and VIS also exhibit sharp-line Yb^{3+} luminescence around 10000 cm^{-1} .

Figure 4 shows the 15 K NIR excitation spectrum of the broad VIS luminescence. It essentially consists of a superposition of the two spectra in Figure 2, an indication that both Yb^{3+} sites A and B contribute to the Mn^{2+} luminescence.

Figure 5 shows the polarized absorption spectra at 15 K of $\text{Rb}_2\text{MnCl}_4:\text{Yb}^{3+}$ in the VIS and the near-UV. All the bands are readily assigned to Mn^{2+} excitations in a somewhat distorted octahedral chloride coordination. A weak broad feature at about 25000 cm^{-1} is likely due to a small Yb^{2+} impurity.

Figure 6 shows the normalized luminescence intensities of the $\text{Mn}^{2+} {}^4\text{T}_{1g} \rightarrow {}^6\text{A}_{1g}$ transition as a function of temperature excited at (a) 10910 cm^{-1} (site A/ Yb^{3+}) and (b) 19455 cm^{-1} . Both show a steep drop between 30 and 100 K. The drop of the UC luminescence starts at 35 K, whereas the directly excited Mn^{2+} starts to drop at 50 K.

Figure 7 shows the VIS/NIR ratio of emitted photons as a function of temperature for site A excitation at 10910 cm^{-1} (7a)

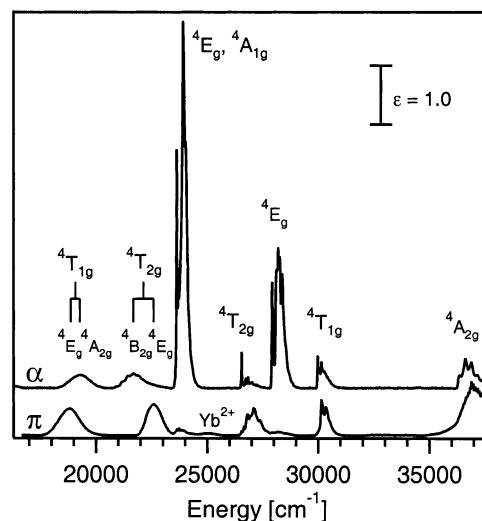


Figure 5. α and π polarized absorption spectra of a single crystal of $\text{Rb}_2\text{MnCl}_4:\text{Yb}^{3+}$. All transitions are labeled in O_h notation. The splitting of the ${}^4\text{T}_{1g}$ and the ${}^4\text{T}_{2g}$ bands in D_{4h} is indicated. ϵ is given in $\text{l}\cdot\text{mole}^{-1}\cdot\text{cm}^{-1}$.

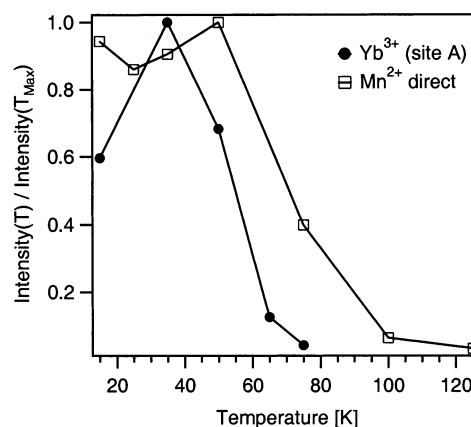


Figure 6. Normalized luminescence intensities of the $\text{Mn}^{2+} {}^4\text{T}_{1g} \rightarrow {}^6\text{A}_{1g}$ transition as a function of temperature for excitation energies of (a) 10910 cm^{-1} and (b) 19455 cm^{-1} . The luminescence intensities are normalized to 1 at 35 K for (6a) and 50 K for (6b).

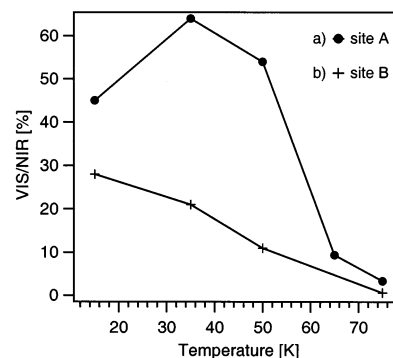


Figure 7. Temperature dependence between 15 and 75 K of the VIS/NIR ratio of emitted photons for excitation energies of (a) 10910 cm^{-1} (site A) and (b) 10777 cm^{-1} (site B) at an excitation power of 191 mW.

and site B excitation at 10777 cm^{-1} (7b). This ratio is very high, particularly for site A at temperatures of 50 K and below. For the laser power 191 mW used in this experiment, the VIS/NIR emitted photon ratio for site A excitation at 50 K and below is about 1/2. The VIS/NIR photon ratio decreases between 15 and 75 K by factors of 13 and 42 for sites A and B, respectively.

4. Discussion

4.1 Yb³⁺ Sites. Rb₂MnCl₄ is a tetragonal two-dimensional perovskite and crystallizes in the space group *I4/mmm* with *a* = 5.05 Å, *c* = 16.14 Å, and *Z* = 2.²⁶ It contains layers of corner-sharing [MnCl₆]⁴⁻ octahedra. The Mn²⁺ centers have local *D*_{4h} symmetry with the nearest neighbors separated by 5.05 Å within and 8.84 Å between the layers. Rb₂MnCl₄ is a 2D-antiferromagnet below *T*_N = 57 K, with a nearest-neighbor exchange parameter *J* = 4.3 cm⁻¹ ($\vec{H}_{\text{ex}} = \vec{J}\vec{S}_1 \cdot \vec{S}_2$).²⁸

Two major Yb³⁺ sites are immediately identified from the luminescence and excitation spectra in Figures 1 and 2. Sites A and B can be selectively excited at 10910 and 10777 cm⁻¹, respectively. The spectra in Figures 1 and 2 have the typical energy and appearance of ²F_{7/2} ↔ ²F_{5/2} transitions of Yb³⁺. Apparently, most of the intensity lies in the electronic origins, thus indicating a lack of a symmetry center in both sites. It is not possible to unambiguously assign the lines to specific crystal-field (CF) components and thus determine the CF splitting in the ²F_{7/2} and ²F_{5/2} states. This is mainly due to the occurrence of vibronic sidebands which cannot be distinguished from electronic origins. Some luminescence and excitation lines consist of several components; see Figures 1 and 2. We attribute this to two factors. One is valid for both sites: at 15 K the host lattice Rb₂MnCl₄ is antiferromagnetically ordered. The Yb³⁺ ions are thus exposed to an internal field, resulting in a Zeeman splitting of the relevant *f*–*f* levels. The second factor applies to site A only. The fine structure is richer with many more components for the site A spectra than the site B in Figures 1 and 2. This is attributed to the presence of two very similar subsites A1 and A2 within site A. We also note from Figure 1 that excitation energy transfer between the sites at 15 K is negligible. The slight contamination of site B excitation in the site A spectrum of Figure 2a is due to a nonzero site A luminescence at the detection energy of 10152 cm⁻¹ in this experiment.

Incorporation of a trivalent ion into Rb₂MnCl₄ requires some charge compensation and this leads to disorder in the structure. This is the likely reason for the very low Yb³⁺ concentration of <0.1 mol % in our crystals. In Figure 8, we have drawn four plausible Yb³⁺ sites in Rb₂MnCl₄ including the local charge compensation. The Yb³⁺ ion has an ionic radius of 0.87 Å, very similar to 0.83 Å for Mn²⁺. Yb³⁺ thus likely substitutes for Mn²⁺. In Figure 8b, the charge is compensated by a nearby Rb⁺ vacancy. In Figure 8c, a Cl⁻ ion is replaced by O²⁻ adjacent to Yb³⁺. Despite the great care in the synthesis, we cannot exclude the presence of traces of O²⁻ or OH⁻ ions in the melt. In Figure 8a₁ and 8a₂, two Yb³⁺ ions are arranged around a Mn²⁺ vacancy. The only difference is that in 8a₁ the Yb³⁺–vacancy–Yb³⁺ arrangement is linear, whereas in 8a₂ it is a 90° arrangement. A preference for M³⁺–vacancy–M³⁺ sites is found in M³⁺ doped ABX₃ lattices with face-sharing BX₆ chains.^{29,30} In our case, the octahedra are corner-sharing within the *a*–*b* plane of the tetragonal lattice. An arrangement as shown in 8a₁ or 8a₂ appears plausible also in this situation.

In all the situations drawn in Figure 8, the Yb³⁺ ions have linear Yb³⁺–Cl⁻–Mn²⁺ bridging geometry to several nearest neighbors in the *ab*-plane of the lattice. It will be shown below that this bridging arrangement is a key to understanding the photon upconversion mechanism and the high efficiency of the process. We cannot unambiguously assign our empirically determined spectroscopic sites A₁, A₂, and B to the structural sites in Figure 8. However, it is plausible to assign the two sites A₁ and A₂, which are spectroscopically almost identical and

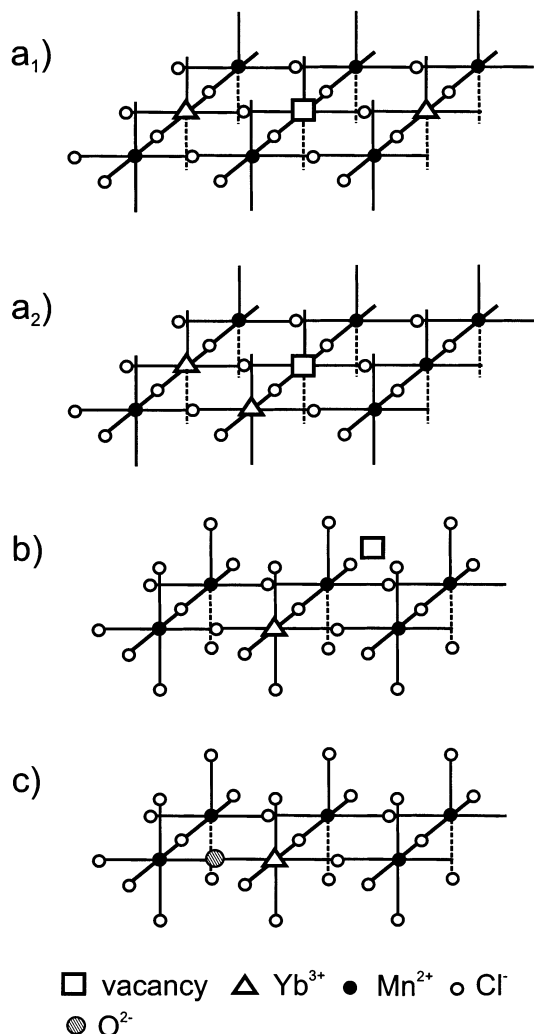


Figure 8. Relevant fragments of the Rb₂MnCl₄:Yb³⁺ crystal structure illustrating the different Yb³⁺ substitution patterns with charge-compensating vacancies. The Yb³⁺ ions have linear Yb³⁺–Cl⁻–Mn²⁺ bridging geometry to several nearest neighbors in the *a*–*b* plane of the lattice. In (c) a Cl⁻ ion is replaced by O²⁻ adjacent to Yb³⁺.

can only be distinguished because of the high resolution of our spectroscopy, to the sites shown in Figure 8a₁ and 8a₂, respectively. We would expect essentially the same crystal-field splittings for the two.

4.2 Upconversion Mechanism. The fact that ²F_{7/2} → ²F_{5/2} excitation of Yb³⁺ around 1 μm leads to intense yellow-orange ⁴T_{1g} → ⁶A_{1g} luminescence of Mn²⁺ in Rb₂MnCl₄:Yb³⁺ is remarkable. We have observed similar phenomena in RbMnCl₃:Yb³⁺, CsMnCl₃:Yb³⁺, and CsMnBr₃:Yb³⁺. However, in none of these have we achieved as high VIS/NIR photon ratios as in the present case. In this section, we discuss possible mechanisms for the unusual phenomenon, and in section 4.3 the efficiency question will be addressed. Photon upconversion (UC) is a well-documented phenomenon in lanthanide-doped materials, and several mechanisms have been proposed to account for the observed behavior in these systems. In Figure 9a, 9b, and 9c, three important ones are schematically represented. In Figure 9a, the emitting state is reached by a sequence of ground-state absorption (GSA) and excited-state absorption (ESA) steps. This GSA/ESA sequence occurs on a single lanthanide ion. This mechanism is characterized by the following features: The excitation spectrum corresponds to the product of the GSA and ESA spectra, and the UC intensity decays immediately after a short excitation pulse. Figure 9b shows the most important

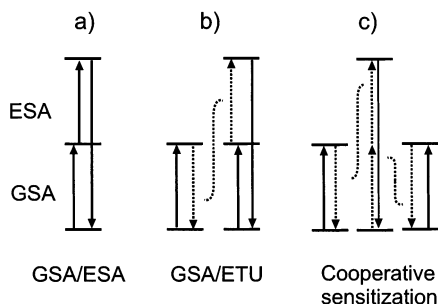


Figure 9. Schematic representation of photon upconversion mechanisms. GSA denotes ground-state absorption and ESA excited-state absorption. Full arrows correspond to radiative transitions and dashed arrows represent nonradiative processes.

mechanism in lanthanide compounds: Two ions in close proximity are excited to the intermediate state in the first step. UC is then achieved by an energy-transfer (ET) step, in which one ion ends up in the emitting state and the other one in the ground state. This GSA/ETU mechanism is characterized by an excitation spectrum corresponding to the square of the GSA spectrum. A short excitation pulse deposits the excitation in the intermediate state, and the UC luminescence transient typically shows a measurable rise followed by a decay. Figure 9c corresponds to a three-center process and is not common in lanthanide systems. It is included here because it is a potential candidate for the situations in Figure 8a₁ and 8a₂, where two Yb^{3+} ions are bound together by their common charge-compensating vacancy. In Figure 9c, two donor ions in proximity to an acceptor ion are both excited in the first step, and in the second step they simultaneously transfer their excitation to the acceptor. This mechanism is characterized by an excitation spectrum corresponding to the square of GSA, and for pulsed excitation the transient shows a rise followed by a decay.

The temporal evolution of the Mn^{2+} luminescence intensity at 15 K following a 10 ns excitation pulse into a Yb^{3+} absorption at 10202 cm^{-1} clearly shows that there is no rise in the UC transient. There is an immediate single exponential decay after the excitation pulse, corresponding to a lifetime of 9.7 ms. Thus, there is no slow energy-transfer step, and this immediately eliminates the GSA/ETU and the cooperative sensitization mechanisms in Figure 9b and 9c, respectively. Both the GSA and the UC process must occur during the laser pulse. This points to a GSA/ESA sequence. However, a normal GSA/ESA mechanism in lanthanide systems occurs on a single ion, which is clearly impossible in $\text{Rb}_2\text{MnCl}_4\text{:Yb}^{3+}$. Yb^{3+} has only one excited state around 10000 cm^{-1} , and Mn^{2+} has no excited states below 17000 cm^{-1} ; see Figure 5. The primary excitation is clearly a ${}^2\text{F}_{7/2} \rightarrow {}^2\text{F}_{5/2}$ GSA on Yb^{3+} , while the luminescence is due to ${}^4\text{T}_{1g} \rightarrow {}^6\text{A}_{1g}$ on Mn^{2+} . Thus, our process is cooperative, involving both Yb^{3+} and Mn^{2+} ions. We choose the most simple model to explain it: a nearest-neighbor $\text{Yb}^{3+}\text{—Cl}^- \text{—Mn}^{2+}$ dimer. The real situation is of course more complicated because each Yb^{3+} has more than one nearest-neighbor Mn^{2+} and, in addition, the Rb_2MnCl_4 lattice is magnetically ordered below 57 K. A dimer already provides the essential condition for the two optically relevant ions Yb^{3+} and Mn^{2+} . There is evidence in Figure 3 that the upconversion process is a localized $\text{Yb}^{3+}/\text{Mn}^{2+}$ cooperative process at 15 K. Direct Mn^{2+} excitation in the green results in a very similar luminescence spectrum (Figure 3a) to UC excitation of site A Yb^{3+} (Figure 3b). Site B excitation, on the other hand, leads to a Mn^{2+} luminescence which is red-shifted by about 340 cm^{-1} . It is known from earlier spectroscopic studies of Rb_2MnCl_4 that at 15 K there is no extensive

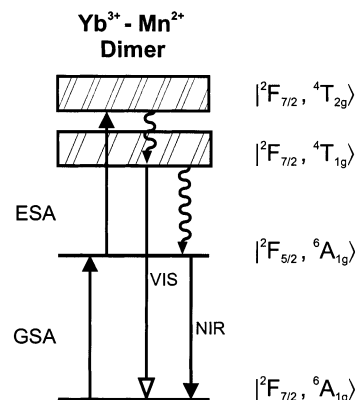


Figure 10. Schematic representation of the photon upconversion process in a $\text{Yb}^{3+}\text{—Mn}^{2+}$ dimer. Full arrow lines and curly arrows represent radiative and nonradiative processes, respectively. The states are labeled in a $\text{Yb}^{3+}\text{—Mn}^{2+}$ dimer notation.

${}^4\text{T}_{1g}$ excitation energy migration in this lattice.³¹ From Figure 3 we can thus conclude that at 15 K Mn^{2+} luminescence occurs from Mn^{2+} ions in the neighborhood of the Yb^{3+} ions which are involved in the excitation process. These neighborhoods are different for Yb^{3+} sites A and B and thus for the shift of Mn^{2+} luminescence band. The red-shift in site B indicates an overall stronger crystal field of the emitting Mn^{2+} than in site A.

Figure 10 shows the relevant states and processes in our dimer model. The dimer states have a double label according to the state of each partner in a given dimer state. $|{}^2\text{F}_{5/2}, {}^6\text{A}_{1g}\rangle$ is thus a ${}^2\text{F}_{5/2}$ excited state of Yb^{3+} , which is slightly perturbed by the Mn^{2+} neighbor. Both the $|{}^2\text{F}_{7/2}, {}^6\text{A}_{1g}\rangle \rightarrow |{}^2\text{F}_{5/2}, {}^6\text{A}_{1g}\rangle$ GSA and the $|{}^2\text{F}_{7/2}, {}^4\text{T}_{1g}\rangle \rightarrow |{}^2\text{F}_{7/2}, {}^6\text{A}_{1g}\rangle$ luminescence are essentially localized transitions, the former on Yb^{3+} and the latter on Mn^{2+} . Confirmation that the luminescence transition is not strongly perturbed by the presence of Yb^{3+} is provided by the very similar Mn^{2+} luminescence band shapes and lifetimes for direct Mn^{2+} excitation at 18797 cm^{-1} and UC excitation at 10202 cm^{-1} : 7.9 ms and 9.7 ms, respectively. The crucial step in Figure 10 is the $|{}^2\text{F}_{5/2}, {}^6\text{A}_{1g}\rangle \rightarrow |{}^2\text{F}_{7/2}, {}^4\text{T}_{2g}\rangle$ ESA step. It takes the dimer from a nominally Yb^{3+} centered state to a nominally Mn^{2+} centered state. In the present system, this must be a very efficient step because it is competitive with the NIR luminescence process of Yb^{3+} .

4.3 Upconversion Efficiency and $\text{Yb}^{3+}\text{—Mn}^{2+}$ Bridging Geometry. We postulate that the ESA step in the dimer model of Figure 10 gains oscillator strength by an exchange mechanism. It is well known that in dimers and higher clusters of transition-metal ions, spin-forbidden transitions, in particular spin-flip transitions, can gain intensity by exchange interactions between the magnetic ions. Enhancement of spin-forbidden bands by up to 3 orders of magnitude have been reported.¹⁶ In Cr^{3+} dimers, cooperative double excitations, corresponding to the simultaneous excitation of both ions by a single photon, can be very prominent in the absorption spectrum.³² In the present case, the relevant exchange coupling is between the lanthanide ion Yb^{3+} and the transition-metal ion Mn^{2+} . Their respective electron configurations are $4f^{13}$, corresponding to one hole in the full 4f shell, and $3d^5$, that is, one unpaired electron in each of the five d orbitals.

Tanabe and co-workers established a formalism to account for the observed enhancement of spin-forbidden transitions in magnetically coupled transition-metal ion compounds.³³ This was successfully applied to magnetically coupled spin clusters of Mn^{2+} , Ni^{2+} , and Cr^{3+} ^{34–36} as well as magnetically ordered materials.³⁷ It was also invoked to explain some unusual

TABLE 1: Experimental Upconversion Efficiencies η_{UC} (according to Eq 2) Normalized to a Laser Power of 191 mW

compound	temperature [K]	efficiency [%]	
Rb ₂ MnCl ₄ :Yb ³⁺	35	28 (site A)	corner-sharing
Rb ₂ MnCl ₄ :Yb ³⁺	15	18 (site B)	corner sharing
CsMnCl ₃ :Yb ³⁺ ²³	75	8.5	corner-sharing
RbMnCl ₃ :Yb ³⁺ ²¹	10	2	corner-sharing
RbMnCl ₃ :Yb ³⁺ ²¹	10	0.02	face-sharing
CsMnBr ₃ :Yb ³⁺ ²⁴	12	0.05	face-sharing

cooperative transitions in Cr³⁺ doped EuAlO₃ crystals.³⁸ This latter example is relevant for our discussion because it is a mixed lanthanide–transition-metal system. Besides the normal R lines corresponding to ²E → ⁴A₂ transitions on Cr³⁺ single ions, very intense red-shifted lines were found in the luminescence spectrum. The authors of reference 38 convincingly showed that in the final state of these transitions the Eu³⁺ ions were not in the ⁷F₀ ground state but in excited ⁷F_J states. The analogy to our present situation is evident: an excitation on one ion is coupled to a de-excitation of the partner; see the ESA step in Figure 10. A dimer model of exchange-coupled ions appears to be perfectly appropriate to account for such effects, even in situations which are physically more complicated.

The measured ratio of VIS/NIR emitted photons is a reasonable measure of the upconversion efficiency as long as this ratio is not too high. As we see in Figure 7, a VIS/NIR ratio of 64% is achieved in the title compound at 35 K for site A excitation. In this situation, it is more appropriate to define a UC quantum efficiency as follows:

$$\eta_{UC} = \frac{VIS_{out}}{NIR_{abs}} \quad (1)$$

In our Yb³⁺–Mn²⁺ system at low temperatures this can be approximated by

$$\eta_{UC} \approx \frac{VIS_{out}}{NIR_{out} + 2VIS_{out}} \quad (2)$$

Equation 2 is based on the assumption that there are no nonradiative processes depleting the |²F_{5/2}, ⁶A₁) and |²F_{7/2}, ⁴T₁) levels. This is valid at 50 K and below but not at higher temperatures; see section 4.4.

η_{UC} as defined in eq 2 can reach a maximum value of 0.5, corresponding to the situation when all the absorbed NIR photons are nonlinearly transformed to VIS photons. In Table 1, we compare experimentally determined η_{UC} values for various Yb³⁺ doped Mn²⁺ halide compounds at low temperatures, where the assumptions of eq 2 are valid. The UC efficiency is, of course, dependent on the laser power because the UC process is nonlinear, whereas the NIR luminescence process is linear. The η_{UC} values in Table 1 are all scaled to a laser power of 191 mW and thus are comparable. We notice orders of magnitude differences of η_{UC} in Table 1. The largest values of 8.5% and 28% are found in CsMnCl₃:Yb³⁺ and Rb₂MnCl₄:Yb³⁺, respectively. The smallest η_{UC} = 0.02% and η_{UC} = 0.05% are found in RbMnCl₃:Yb³⁺ (face-sharing site) and CsMnBr₃:Yb³⁺, respectively.

The linear Yb³⁺–Cl[–]–Mn²⁺ bridging geometry is evidently most efficient in inducing intensity of cooperative transitions. In our case, it is the ESA step in Figure 10, the second step in the upconversion excitation of the Yb³⁺–Mn²⁺ pair. This must be exchange induced for two principal reasons. In Rb₂MnCl₄:Yb³⁺, the Yb³⁺–Mn²⁺ distance is 5.05 Å, whereas in CsMnBr₃:

Yb³⁺, where the UC efficiency is 3 orders of magnitude smaller, it is 3.26 Å. If the UC process was due to electric multipole–multipole interactions, the distance dependence of the efficiency would be opposite. An energy-transfer process due to an electric dipole–dipole mechanism has an R^{–6} dependence. This would lead to an order of magnitude increase between Rb₂MnCl₄:Yb³⁺ and CsMnBr₃:Yb³⁺. In addition, such a process would likely be slower than the laser pulse and lead to a rise in the UC transient, which is not observed. Also, the very high absolute efficiency of the UC process in the title compound at 15 K is not compatible with a mechanism other than exchange.^{36,38} The experimentally observed behavior thus clearly shows the dominant exchange mechanism across the linear Yb³⁺–Cl[–]–Mn²⁺ bridge. We are presently exploring ways to an understanding of the exchange-induced UC mechanism on a more fundamental level. This turns out to be nontrivial, however, for two main reasons. The calculation of orbital exchange parameters between transition-metal and lanthanide ions is much less explored than between two transition-metal ions.³⁹ The second problem is the translation of the ground-state exchange parameters thus obtained into intensity parameters.³³ For this comparative study, we are including Yb³⁺–Mn²⁺ systems with corner-sharing, edge-sharing, and face-sharing octahedral connections.

4.4 Loss Mechanisms above 50 K. As shown in Figures 6 and 7, both the VIS luminescence intensity and the VIS/NIR intensity ratio upon NIR excitation drop significantly above 50 K. From a materials point of view, this is disappointing for a material with such an unusually high UC efficiency at low temperatures. The drop occurs at significantly lower temperatures than in the related CsMnCl₃:Yb³⁺ and RbMnCl₃:Yb³⁺ systems.

We can identify three loss processes, one of which is intrinsic for Rb₂MnCl₄, whereas the other two are directly related to the presence of Yb³⁺ ions in the crystal. Figure 6 shows that there is a steep drop of the ⁴T_{1g} → ⁶A_{1g} luminescence intensity above 50 K for direct Mn²⁺ excitation into ⁴T_{1g}. A similar behavior has been observed and described for pure Rb₂MnCl₄.²⁷ As in CsMnCl₃ and RbMnCl₃,⁴⁰ it was described as energy migration to killer traps.

The migration is thermally activated, and the activation energy is significantly lower in Rb₂MnCl₄ than in the other two lattices. The most likely killer traps are Fe³⁺ and Mn³⁺ ions. The migration can be slowed and the activation energy raised by a reducing atmosphere in the crystal growth.⁴¹ This principle does unfortunately not work for our Yb³⁺ doped compounds. A reducing atmosphere has shown to reduce Yb³⁺ to Yb²⁺.²¹ The thermal activation of the Mn²⁺ to Mn²⁺ energy transfer has two main reasons: (1) The antiferromagnetic order (T_N = 57 K in Rb₂MnCl₄), which prohibits transfer between nearest neighbors at low temperatures, and (2) the reduced metal–ligand distances of the (MnCl₆)^{4–} octahedron in the ⁴T_{1g} emitting state lead to a large Stokes shift and a very small spectral overlap at low temperatures. Both are likely to play a role in the intrinsic loss of luminescence intensity with increasing temperature in Rb₂MnCl₄. In addition to these intrinsic loss processes, there are two additional processes leading to luminescence loss in Yb³⁺ doped Rb₂MnCl₄. One can be identified by inspection of Figure 6. In the same crystal, the thermal quenching of Mn²⁺ luminescence sets in at lower temperature for UC excitation than for direct Mn²⁺ excitation. This is related to the fact, see also section 4.1 and Figure 3, that the Mn²⁺ ions participating in UC are slightly perturbed by the neighboring Yb³⁺ ions and vacancies. As a consequence, their thermally activated multiphonon relaxation is somewhat more efficient. The second

process is shown by the long curly arrow in Figure 10. In the dimer picture, it is a nonradiative relaxation process from $|^2\text{F}_{7/2}, ^4\text{T}_{1g}\rangle$ to $|^2\text{F}_{5/2}, ^6\text{A}_{1g}\rangle$. This energy gap is small and the corresponding potentials are displaced, leading to a thermal activation.

All of these loss processes at high temperatures are governed by basic physical laws. There is therefore no obvious way to engineer a material containing Yb^{3+} and Mn^{2+} which could be used as an upconverter at room temperature on the basis of the principles described here. The intrinsic loss process can in principle be reduced by diluting the Mn^{2+} ions in a host lattice, but the last loss process described above cannot be eliminated. We are presently exploring the possibility to codope Yb^{3+} and Cr^{3+} ions in an oxide host lattice for upconversion processes based on the same principle. The advantage in these is the spin—flip nature of the $\text{Cr}^{3+} \text{ } ^2\text{E}_g$ luminescence, which should render the last loss process described above less likely.

Acknowledgment. The authors are grateful to Pascal Gerner for helpful discussions. This work was financially supported by the Swiss National Science Foundation.

References and Notes

- (1) Auzel, F. *Acad. Sci. Paris* **1966**, 1016.
- (2) Wright, J. C. *Topics in Applied Physics: Radiationless Processes in Molecules and Condensed Phases*; Fong, F. K., Ed.; Springer: Berlin, 1976; pp 239–295.
- (3) Jüstel, T.; Nikol, H.; Ronda, C. *Angew. Chem.* **1998**, *110*, 3250.
- (4) Lenth, W.; Macfarlane, R. M. *Opt. Photon News* **1992**, *3*, 8.
- (5) Downing, E.; Hesselink, L.; Raltson, J.; McFarlane, R. *Science* **1996**, *273*, 1185.
- (6) Hehlen, M. P.; Krämer, K.; Güdel, H. U.; McFarlane, R. A.; Schwartz, R. N. *Phys. Rev. B* **1994**, *49*, 12475.
- (7) Thrash, R. J.; Johnson, L. F. *J. Opt. Soc. Am. B* **1994**, *11*, 881.
- (8) Wenger, O. S.; Gamelin, D. R.; Güdel, H. U.; Butashin, A. V.; Kaminskii, A. A. *Phys. Rev. B* **2000**, *61*, 16530.
- (9) Mujaji, M.; Jones, G. D.; Syme, R. W. G. *J. Lumin.* **1992**, *53*, 473.
- (10) Kamo, T.; Yamamoto, H.; Yoshiro, O. *J. Electrochem. Soc.* **1972**, *119*, 1561.
- (11) Riedener, T.; Güdel, H. U. diploma thesis, University of Bern, Bern, 1992.
- (12) Krämer, K.; Güdel, H. U. *Phys. Rev. B* **1997**, *56*, 13830.
- (13) Joubert, M. F.; Guy, S.; Cueurq, S.; Tanner, P. A. *J. Lumin.* **1997**, *75*, 287.
- (14) Wermuth, M.; Riedener, T.; Güdel, H. U. *Phys. Rev. B* **1998**, *57*, 4369.
- (15) Müller, P.; Wermuth, M.; Güdel, H. U. *Chem. Phys. Lett.* **1998**, *147*, 105.
- (16) Jacobsen, S. M.; Güdel, H. U. *J. Lumin.* **1989**, *43*, 125.
- (17) Oetliker, U.; Riley, M. J.; May, P. S.; Güdel, H. U. *Coord. Chem. Rev.* **1991**, *111*, 125; see also references therein.
- (18) Gamelin, D. R.; Güdel, H. U. *J. Am. Chem. Soc.* **1998**, *120*, 12143.
- (19) Gamelin, D. R.; Güdel, H. U. *Inorg. Chem.* **1999**, *38*, 5154.
- (20) Wermuth, M.; Güdel, H. U. *J. Am. Chem. Soc.* **1999**, *121*, 10102.
- (21) Valiente, R.; Wenger, O.; Güdel, H. U. *Phys. Rev. B* **2001**, *63*, 165102.
- (22) Valiente, R.; Wenger, O.; Güdel, H. U. *Chem. Phys. Lett.* **2000**, *320*, 639.
- (23) Valiente, R.; Wenger, O. S.; Güdel, H. U. *J. Chem. Phys.* **2002**, *116*, 5196.
- (24) Gerner, P.; Valiente, R.; Wenger, O.; Güdel, H. U. *Inorg. Chem.* **2001**, *40*, 4534.
- (25) Heer, S.; Wermuth, M.; Krämer, K.; Güdel, H. U. *Chem. Phys. Lett.* **2001**, *334*, 293.
- (26) Goodyear, J.; Ali, E. M.; Steigmann, G. A. *Acta Crystallogr.* **1977**, *B33*, 2932.
- (27) Kambli, U.; Güdel, H. U.; Briat, B. *J. Phys. C: Solid State Phys.* **1984**, *17*, 3113.
- (28) Epstein, A.; Gurewitz, E.; Makovsky, J.; Shaked, H. *Phys. Rev.* **1971**, *B2*, 3703.
- (29) McPherson, G. L.; Henling, L. W. *Phys. Rev. B* **1977**, *16*, 1889.
- (30) Henling, L. W.; McPherson, G. L. *Phys. Rev. B* **1977**, *16*, 4756.
- (31) Kambli, U.; Güdel, H. U. *Inorg. Chem.* **1984**, *23*, 3479.
- (32) Güdel, H. U. *Comments Inorg. Chem.* **1984**, *3*, 189.
- (33) Ferguson, J.; Guggenheim, H. J.; Tanabe, Y. *J. Phys. Soc. Jpn.* **1966**, *21*, 692.
- (34) Tsujikawa, I. *J. Phys. Soc. Jpn.* **1963**, *18*, 1391.
- (35) Hoekstra, H. J. W. M.; Ronda, C. R.; Haas, C. *Physica* **1983**, *122B*, 295.
- (36) van der Ziel, J. P. *J. Chem. Phys.* **1972**, *57*, 2442.
- (37) Fujiwara, T. *J. Phys. Soc. Jpn.* **1973**, *34*, 1180.
- (38) van der Ziel, J. P.; van Uitert, L. G. *Phys. Rev.* **1969**, *180*, 343.
- (39) Hay, J. P.; Thibault, J. C.; Hoffmann, R. J. *Am. Chem. Soc.* **1975**, *97*, 4884.
- (40) Kambli, U.; Güdel, H. U. *J. Phys. C: Solid State Phys.* **1984**, *17*, 4041.
- (41) McPherson, G. L.; Talluto, K.; Auerbach, R. A. *Solid State Commun.* **1982**, *43*, 817.